Earth Planet. Sci. Lett. 686 (2026) 120041

Contents lists available at ScienceDirect

Earth and Planetary Science Letters

journal homepage: www.elsevier.com/locate/epsl

What triggered the catastrophic 15 January 2022 Hunga eruption?

Jie Wu [a,b,1,*], Shane J. Cronin [a,1,*], Marco Brenna [b,*], Joali Paredes-Mariño [a], Sung-Hyun Park [c], Mila Huebsch [a], Alessio Pontesilli [d], Chris Firth [e], David Adams [a], Teresa Ubide [f], Kyle Hamilton [e], Alice MacDonald [f,g], Enrico Califano [b,h], James D.L. White [b], Terry Plank [i], Marta Ribó [j], Ingrid Ukstins [a], Frank Ramos [k], Silvio Mollo [h], Jihyuk Kim [c,l], Folauhola Latu'ila [m], Taaniela Kula [m], Renne Vaiomounga [m]

[a] School of Environment, University of Auckland, Auckland, 1010, New Zealand
[b] Department of Geology, University of Otago, Dunedin, 9054, New Zealand
[c] Korea Polar Research Institute, Incheon, 21990, Republic of Korea
[d] Istituto Nazionale di Geofisica e Vulcanologia, Rome, 00143, Italy
[e] School of Earth & Atmospheric Sciences, Queensland University of Technology, Brisbane, 4001, Australia
[f] School of the Environment, University of Queensland, Brisbane 4000, Australia
[g] Centre for Ore Deposits and Earth Sciences, University of Tasmania, Hobart 7005, Australia
[h] Department of Earth Sciences, Sapienza, University of Rome, Rome 00185, Italy
[i] Department of Earth and Environmental Sciences, Columbia University, NY, 10027, USA
[j] School of Science, Auckland University of Technology, Auckland 1010, New Zealand
[k] Department of Geological Sciences, New Mexico State University, Las Cruces, USA
[l] Department of Earth Science Education, Pusan National University, Busan 46241, Republic of Korea
[m] Tonga Geological Services, Nuku'alofa, Kingdom of Tonga

ARTICLE INFO

Editor: Dr R. Hickey-Vargas

Keywords:
Hunga volcano
Eruption trigger
Magma reservoir
Magma decompression
Glass chemistry
Edifice weakening

ABSTRACT

The 15 January 2022 eruption of Hunga caldera volcano was the most explosive volcanic event in the last 140 years, yet the erupted composition was similar to historical smaller-scale eruption episodes at this center. By analyzing the petrology and geochemistry of the full pyroclastic sequence, we infer the presence of two distinct magma storage zones. Early Surtseyan eruptions (29 December 2021 to 14 January 2022) tapped a resident shallow magma (A2) similar to the 2009 and 2014–2015 episodes and were of similar magnitude. A sudden increase in eruption magnitude over 16 h on 13–14 January 2022 was accompanied by the first arrival of a slightly more primitive and gas-rich magma (A1), along with sudden vent-subsidence below sea-level. Rapid magma withdrawal, subsidence and deep-fracture formation destabilized the upper magmatic system and allowed vesiculation and seawater penetration before the climactic eruption began ~6 h later. There is no evidence of deep mafic recharge and instead plagioclase rims record a sudden decompression of A1 magma as it moved into the emptying shallow A2 reservoir. The catastrophic 15 January 2022 eruption was thus triggered by the high eruption-rates of depressurizing volatile-rich resident A1 magma, coupled with runaway phreatomagmatism. An overall narrow range of compositions suggests that the Hunga magmatic system is simple, without prolonged magma storage or segregation to produce evolved compositions. More primitive crystals and less-evolved magma appeared for the first time at Hunga in 2022, contrasting with the previous ~1040–1180 CE caldera-formation cycle, which terminated with more-evolved magmas. This may suggest that repeated caldera collapses have reduced the lithostatic load of the edifice and possibly weakened the upper crust, allowing more primitive magmas to erupt.

* Corresponding authors.
E-mail addresses: wujiext@gmail.com (J. Wu), s.cronin@auckland.ac.nz (S.J. Cronin), marco.brenna@otago.ac.nz (M. Brenna).
[1] These authors contributed equally to this work.

https://doi.org/10.1016/j.epsl.2026.120041
Received 28 August 2025; Received in revised form 27 January 2026; Accepted 10 April 2026
Available online 21 April 2026

1. Introduction

On 15 January 2022, Hunga volcano, a submarine composite cone with a summit caldera in the central Tongan Volcanic Arc, generated the most explosive volcanic eruption in the last 140 years (Matoza et al., 2022). The plume overshoot reached >58 km into the mesosphere (Proud et al., 2022) with at least 6.85 ± 0.07 km^3 dense-rock-equivalent magma evacuated (Cronin et al., 2023), and a volcanic explosivity index of 6 (Poli and Shapiro, 2022). The eruption caused widespread impacts, including devastating tsunami in the Kingdom of Tonga (Borrero et al., 2023; Purkis et al., 2023). Over 150 Tg of water was ejected during the event, hydrating the stratosphere by 5% (Millan et al., 2022; Vömel et al., 2022). The erupting magma released a total of 18.8 Tg SO_2, but only ~0.6–0.7 Tg entered the atmosphere (Carn et al., 2022); the majority (>93%) entered the sea directly during magma fragmentation (Wu et al., 2025). Eruption-fed submarine mass flows travelled >110 km (Chaknova et al., 2025), reshaping the seafloor and damaging >150 km of seafloor data cables (Clare et al., 2023; Seabrook et al., 2023).

Hunga volcano predominantly erupts basaltic andesite to andesite magmas (Bryan et al., 1972; Brenna et al., 2022). While historical eruptions were mainly Surtseyan events (<0.05 km^3, Fig. 1; Cronin et al., 2017; Colombier et al., 2018; Garvin et al., 2018), much larger caldera-forming events have also occurred (Brenna et al., 2022). Highly explosive caldera eruptions occur infrequently from many similar basaltic to andesitic caldera systems [e.g., Yankahe, Vanuatu (Firth et al., 2015); Tofua, Tonga (Caulfield et al., 2011), and Masaya, Nicaragua (Pérez and Freundt, 2006)], but the 2022 Hunga eruption offers the only witnessed example. This provides a unique benchmark to investigate the relationship between magmatic drivers and volcano-structural properties that influence extreme magnitude andesitic eruptions. We present the results of a systematic geochemical analysis of pyroclastic samples erupted two weeks before the climax, one day prior, and at eight intervals during the 11-hour climactic episode on 15 January 2022. This sample resolution provides a rare insight into the initiation of major caldera-forming eruptions and new insights into mafic-intermediate magma reservoir processes driving extreme explosivity.

2. Hunga volcano 2021–2022 eruption sequence and pyroclastic record

Hunga volcano lies along the Tonga-Kermadec intra-oceanic arc, formed by the subduction of the Pacific Plate beneath the Indo-Australian Plate (Schellart et al., 2006; Smith and Price, 2006). The central Tonga Ridge hosts >20 volcanic edifices, and at least seven have erupted since 1770 CE (Simkin and Siebert, 1994), typically forming ephemeral islands of pyroclastic material (Brenna et al., 2022). The small islands of Hunga Tonga and Hunga Ha'apai represent the emergent summit of Hunga volcano and show outward dipping lava and pyroclastic beds that record a formerly larger composite cone that was destroyed during at least two caldera-forming eruptions, one at ~410 to 660 cal. CE (Hall et al., 2025) and another ~1040–1180 cal. CE (Cronin et al., 2017). Small eruptions in 1912, 1937, and 1998 (Bryan et al., 1972; Gatliff et al., 1991) occurred from vents located around the rim of the submerged caldera. In 2009, a 2-month Surtseyan eruption generated base surges, eruption plumes reaching ~7.6 km-high, with a pyroclastic cone of ~0.0176 km^3 that eroded within months (Venzke et al., 2009; Vaughan and Webley, 2010; Brenna et al., 2022). The next eruption, between 19 December 2014 and 24 January 2015 was similar but larger, forming a 2 km-diameter, 120 m-high, ~0.0479 km^3 tephra cone adjacent to Hunga Ha'apai (Global Volcanism Program, 2015; Cronin et al., 2017). Remobilized tephra formed a tombolo connecting the two pre-existing islands (Garvin et al., 2018) which remained until 2022.

The 2021–2022 eruption episode began with Surtseyan eruptions, forming a >8 km-high steam-dominated plume on 19 December 2021 (Gupta et al., 2022). Over the following two weeks, sporadic Surtseyan eruptions occurred from a new vent, ~350 m northeast of the 2015 crater. The eruptions increased in magnitude over time (Fig. 2). From proximal videos and photos on 22 December 2021, sporadic and repetitive individual Surtseyan explosions occurred with pyroclastic jets rising 250–300 m high, and pyroclastic surges radiating up to 600 m from the vent. The plume reached 12 km high (Carn et al., 2022). The next phase of activity during 27–30 December 2021 was similar, but the sporadic pyroclastic jets were higher, reaching 850 m above sea-level

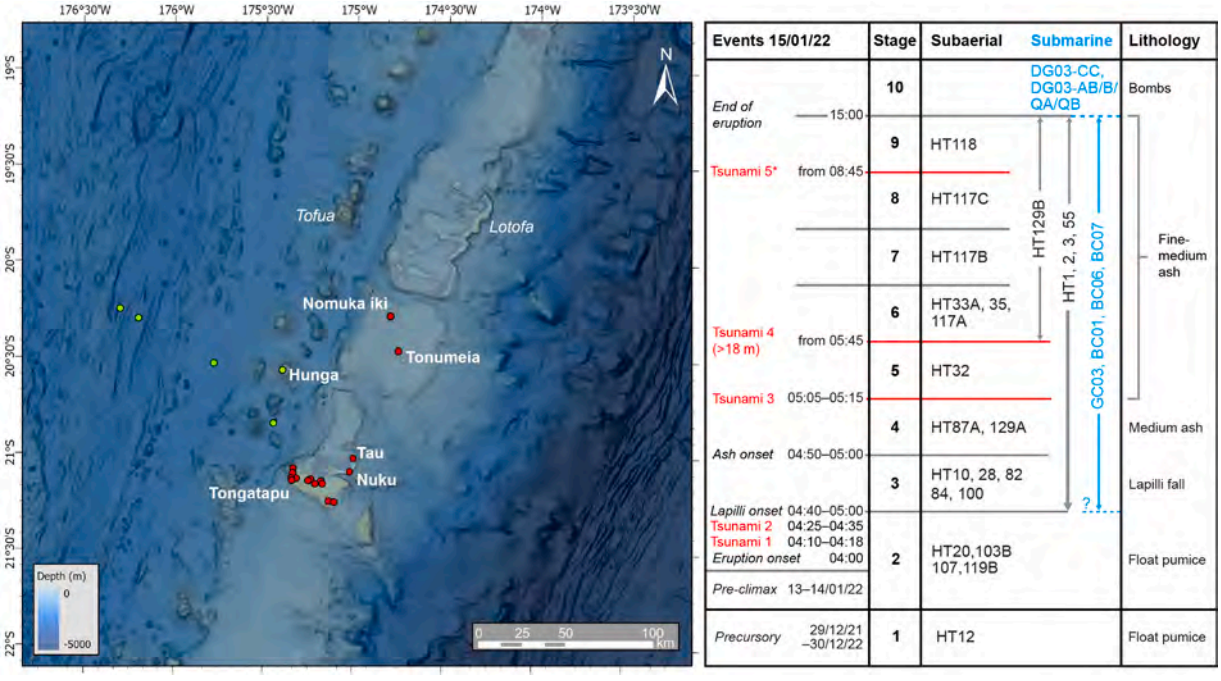

Fig. 1. Map of Hunga volcano and eruption timeline information correlated to samples. Red and yellow circles mark locations for subaerial and submarine samples respectively.

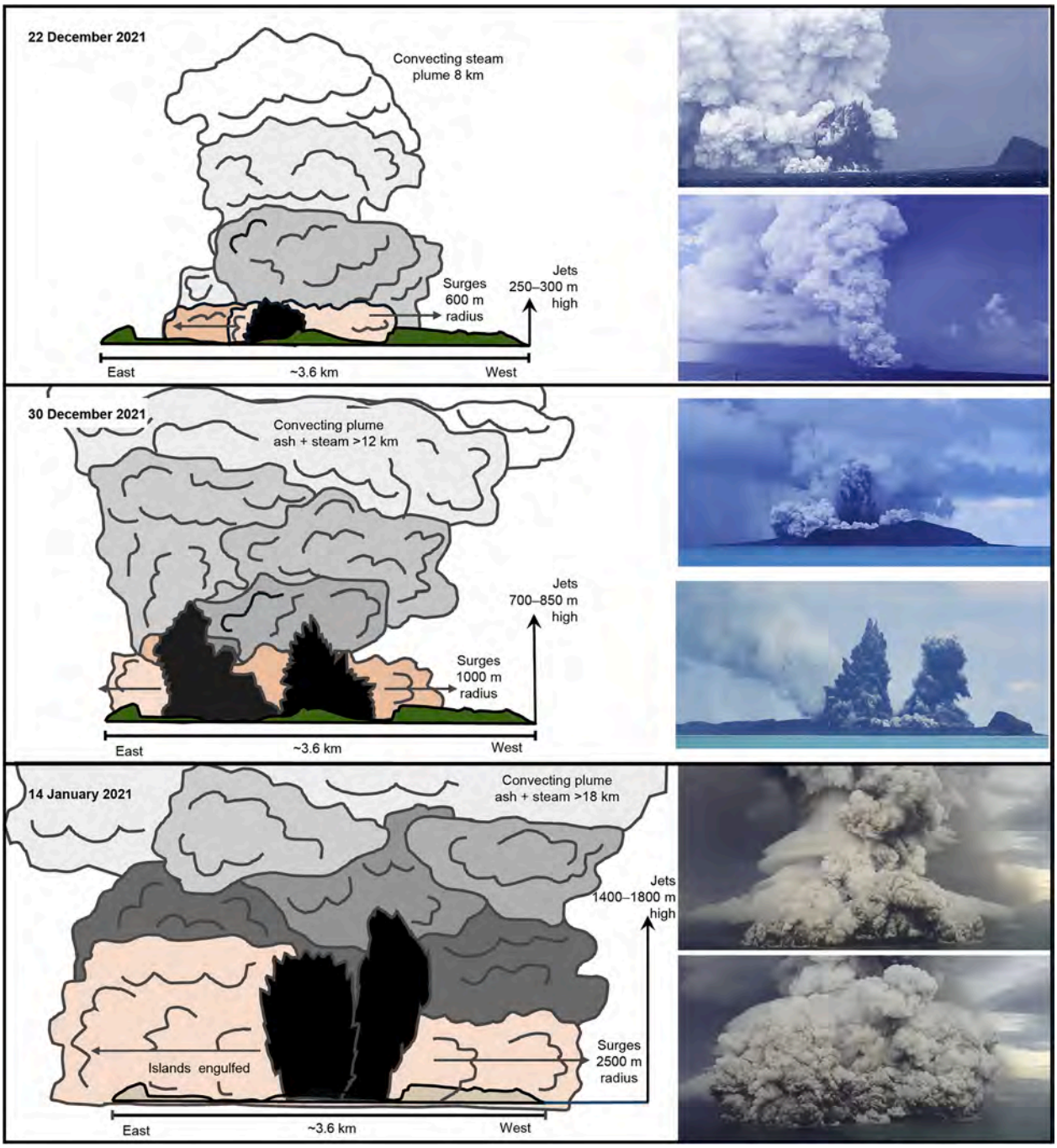

Fig. 2. Precursory eruption scales from eye-witness imagery from 22 December 2021 to 14 January 2022. By comparison the peak of the 15 January 2022 eruption had surges with a ~12 km radius and a plume extending to >50 km high (Mastin et al., 2024).

and surges radiated >1000 m from a vent near water-level (Fig. 2). This was similar to the peak of eruptions observed in 2009 and 2014–2015 (Vaughan and Webley, 2010; Garvin et al., 2018). The 27–30 December 2021 eruptions produced pumice rafts (sampled as Stage 1; Fig. 1) and steam-rich plumes reaching 18 km high (Carn et al., 2022). Pumice from this event washed onto the northern and western beaches of the main populated island of Tongatapu (60–80 km SW) from 7 January 2021. These were sampled as Stage 1; these samples are dark-grey sub-rounded low-density pumice lapilli and bomb fragments, usually showing dark, glassy, bread-crusted margins (HT12; sample details are within Supplementary Table S1).

A 16 h-long period of heightened Surtseyan explosions occurred on 13–14 January 2022, culminating in a 19 km-high steam-rich plume (Fig. 2; Carn et al., 2022), which deposited a few millimeters of fine ash on an overnight ferry passing ~20 km east of the volcano (unfortunately unsampled). Early during this event, the 2014–2022 tuff cone collapsed below sea-level (Wei et al., 2025). Onsite videos show that sporadic, individual Surtseyan eruptions minutes to tens of minutes apart were similar to previous events, but more vigorous, with jets reaching 1400–1800 m high and surges radiating to >2500 m from the vent across the water, leaving floating pumice. A minor pumice raft washed up on Tongatapu and nearby small islands in the last weeks of January 2022. The raft arrival suggests it contains pumice erupted between 13 and 15 January (inclusive). We argue that most of the material, however derives from eruptions during 13–14 January, because the majority of 15 January 2022 pyroclasts were fine-grained (<3 cm lapilli and coarse

ash) and sank rapidly, as reported by Tongan Navy officers ~35 km from the volcano during the eruption. There was no evidence of a persistent pumice raft in satellite images of the tephra footprint of the large eruption on 15 January 2022 (Kelly et al., 2024). Rapid sinking is also consistent with high permeability of the 15 January pumice on-land fall samples. Based on the coarser grain size (>3 cm) and observations of pumice rafts generated during the 13–14 January 2022 explosions, we sampled this rafted pumice as "Stage 2″. We acknowledge that this sample may contain materials of the pre-climax eruption of 13–14 January as well as that from the climactic 15 January eruption. Samples comprise mid to pale-grey, low-density, fine-medium pumice lapilli on beaches of Tongatapu (HT20), Tau (HT103B), Nuku (HT107), and Nomuka-iki (HT119B) islands. The particles commonly show bread-crusted margins, consistent with the Surtseyan eruptions of 13–14 January and that of earlier Stage 1 samples (and 2014–2015 materials; Colombier et al., 2018).

The climactic eruption of Hunga started at ~04:00 (all times in UTC) on 15 January 2022 and lasted ~11 h (Van Eaton et al., 2023). Tephra was collected from intervals timed by observers and sampled intercalated within or above tsunami deposits with observed times of emplacement (Fig. 1). The first satellite view of the eruptive plume was at 04:06 and several observers on or near Tongatapu photographed the early plume at >10 km height at 04:11. A series of vigorous explosions occurred between 04:15 and 04:26 (Matoza et al., 2022; Tarumi and Yoshizawa, 2023) generating globe-encircling atmospheric pressure waves and local sonic booms. These accompanied a rapid transition of the eruption (Fig. 2) during which plume rise and expansion was the fastest ever recorded (Van Eaton et al., 2023; Mastin et al., 2024; Suzuki et al., 2025), and the top of the plume reached >58 km altitude, while the umbrella was around 30 km-high (Proud et al., 2022). The expanding umbrella cloud edge reached Tongatapu from 04:40, and the first tephra fall was deposited between 04:40 and 05:00 (depending on the location). Local interviews, videos and photos show that this initial fall comprised isolated fine lapilli and coarse ash (sampled as Stage 3 on Tongatapu including HT10, 28, 82, 84, 100). The lapilli fall was not long enough to form a complete layer, with roughly 5–10 particles/m^2. Working back from the deposition time, and assuming rise, travel and fall, Stage 3 particles were likely erupted between 04:15 and 04:25, during the plume transformation and acceleration. Subsequent ash fall, minutes after the lapilli fall, comprised coarse-medium ash and was sampled as Stage 4 (HT87A, 129A, forming a ~0.5–1 cm-thick coarse to medium ash unit found at the base of undisturbed fall deposits. The Stage 4 tephra is estimated to have fallen between ~04:50 and 05:15 (depending on location). According to video footage and witness testimonies, the sky darkened due to the plume after ~05:20 (sunset was ~06:20) and subsequently only fine ash fell, with fall steady and slow, reducing and ceasing before ~15:00.

Fall deposits in undisturbed locations on Tongatapu (and also Ha'apai group islands to the north) between ~60 and 140 km from source record a fining upward sequence of medium to fine ash between 1.5 and 4 cm in thickness (Kelly et al., 2024). In order to establish a chronology through the fine ash-dominated portion of the deposit, it was necessary to sample in relation to other known marker horizons (e.g., tsunami deposits) and eye-witness records. On the same islands where tephra was sampled, a series of increasingly large tsunami waves struck the coastal regions, inundating between 50 and 1000 m inland (Borrero et al., 2023).

The tsunami on the Kanokupolu Peninsula (~60 km from source), was timed by eye-witness (interview and video) and instrumental records coupled with tsunami travel time models. Tsunami arrivals at other parts of Tongatapu (e.g., the northern coast protected by reefs) and the islands northwest of Hunga in the Ha'apai group (80–90 km from source) were ~10–15 min later than Kanokupolu, but the order and relative size of waves was the same (Borrero et al., 2023; Purkis et al., 2023; Cronin et al.). At Kanokupolu five tsunami have known timings: Tsunami 1 [Blast 3 waves of Purkis et al. (2023)] struck between 04:10 and 04:18, with a run up of <2 m (Borrero et al., 2023); Tsunami 2 (Blast 4) had a run up of ~3–4 m and struck between 04:25 and 04:35; Tsunami 3 (Blast 5) arrived at ~05:00–5:15 and had a runup of 4–6 m; Tsunami 4, the largest event with >18 m runup (>20 m on Nomuka-iki Island) struck Kanokupolu immediately before 05:45, destroying a weather station and cell-phone tower [timing from Tonga Communications Corporation, reported in Cronin et al.]. Later smaller tsunami are not well recorded due to darkness, ashfall and people having evacuated, although extensive and even ash coverage on Tsunami 4 deposits suggests that subsequent events were small. One later observed event, Tsunami 5* (Blast 6) (Asterix to indicate that there were unknown events between Tsunami 4 and 5*) arrived at ~08:45–09:00 in northern Tongatapu and the southern Ha'apai group islands and had a run up of <3 m on the Kanokupolu Peninsula and Nomuka-iki Island (Borrero et al., 2023; Cronin et al.).

Ash was sampled along the Kanokupolu peninsula and immediately south of it, as well as on the southern Ha'apai islands where the order and relative size of tsunami deposits were mapped by precise surveys and correlated to the Tongatapu sequences (Borrero et al., 2023). Tephra was not found below the tsunami deposits. A 2–3 mm-thick layer of fine black ash was commonly found between deposits of Tsunami 3 and 4 at ~4–6 m above sea-level. This contact is erosive in many places, so the ash is recorded in positions of low flow speed. It was sampled along a Tsunami-survey transect on the western coast of Tongatapu ~3 km south of the Kanokupolu peninsula as Stage 5 (HT32). Tsunami timing and its fine grainsize suggest that Stage 5 tephra was deposited some time after 05:15 and before Tsunami 4 arrived at ~05:45. Tsunami 4 deposits were uniformly covered by ash and tsunami-washed galvanized steel surfaces also had ash fused to them due to salt reacting with the metal surface. The post-Tsunami 4 ash was sampled in a well sheltered location ~20 m above sea-level on the uninhabited Nomuka-iki island (Southern Ha'apai group). At this location Tsunami 4 passed, cleaned the soil surface and deposited a few cm of coral sand. Above the sand, three ~0.5–1 cm-thick fine to medium ash sub-layers (Stages 6–8; HT117A, B, C) were distinguished by textural, sorting and color differences. The last tephra deposited on land comprises a few millimeters of fine ash (Stage 9; HT118) that was deposited above coral sands and debris of Tsunami 5* emplaced at ~09:00. Tsunami 5* deposits on Tongatapu and Nomuka-iki island show a runup of <3 m. Stage 9 ash likely represents an eruptive flare-up at 08:30–09:00 (Tarumi and Yoshizawa, 2023; Van Eaton et al., 2023).

Submarine mass-flow deposits recording eruption-fed currents were sampled west and south of the volcano by RV Araon (Korea Polar Research Institute, KOPRI) in box cores (BC) or gravity cores (GC). <3 cm-thick units 90–110 km west of the volcano (BC01 and BC07) combine pyroclastic material transported by distal mass flow topped by fall deposits (cf., Chaknova et al., 2025). A medial western site (BC06, ~50 km west, 17 cm-thick) and a closer core site (GC03; 30 km-SSW, 115 cm-thick) do not penetrate through the entire sequence. However, a few cores of similar or less depth nearby penetrated all of the 2022 deposit (Clare et al., 2023), and thus the KOPRI cores include most of the eruption sequence. Hydroacoustic signals show that the main eruption-fed mass flows occurred during eruption climax at 04:40–05:05 (Cronin et al.), likely equivalent to Stages 3 and 4. Additional mass flows were also generated during the caldera-collapse episode after 05:30, correlating to Stages 5 and 6, and during eruptive resurgence at 08:30–09:00 (equivalent to Stage 9). The latest sampled phase of the eruption (Stage 10) is represented by pyroclastic bombs (deposited by submarine fountains) and dredged from the southwestern caldera rim.

3. Methods

The Hunga tephra samples were sieved into different size fractions and point counted for componentry. Pumice lapilli and ash from Stages 1–3 and 9 were handpicked and ground into fine powders using agate mortar and pestle for whole-rock major element analyses using X-ray

fluorescence (XRF) at University of Auckland. Tephra samples from each eruptive stage were mounted onto epoxy mounts and polished for electron microprobe analyses (EMPA) of major elements on both volcanic glass and mineral phases (dominantly plagioclase, clinopyroxene, and orthopyroxene with minor olivine) at University of Auckland. Samples from Stages 1–3 were analysed for glass trace elements using LA-ICP-MS at University of Auckland and samples from Stages 3–10 were analysed for glass and groundmass major and trace elements at the University of Queensland. Detailed analytical methods are provided in Supplementary material (Appendix A), and full datasets for whole-rock as well as glass, groundmass, and mineral compositions are provided in the Supplementary Tables S2 to S4 (Appendix B).

4. Results

4.1. Tephra morphology and componentry

Recovered tephra from the 15 January 2022 eruptive phase is dominantly ash (with rare lapilli only during Stage 3), composed of juvenile clasts, crystals (plagioclase and pyroxene) and lithics. Lithics (with weathered, hydrothermally altered, crystalline and non-vesicular textures) comprise <6 vol% of any sample. Juvenile clast particles have fresh angular surfaces, and are divided into three classes: (1) light pumice, (2) dark pumice, and (3) dense blocky glass, along with a small number of banded clasts. From class 1 to 3, juvenile fragments show decreasing vesicularity (Fig. 3a–c). Most juvenile particle types have <7 vol% phenocrysts, dominated by plagioclase (<6 vol%) and pyroxene (<1 vol%, including both clinopyroxene and orthopyroxene) with very rare olivine and magnetite. Groundmass textures range from microlite-poor/free glass (especially in class 3; Fig. 3a–c), to groundmass containing >80 vol.% microlites, dominated by plagioclase and clinopyroxene (typically <100 μm in size; Fig. 3d). Plagioclase, clinopyroxene and orthopyroxene phenocrysts commonly show normal zonation with growth of Ca-poor (in plagioclase) and Mg-poor (in pyroxene) rims. The variable abundance of microlites suggests late-stage (syn/post-eruptive) crystallization. A single volcanic bomb (DG03) from Stage 10 shows inward increasing microlite crystallization, highlighting post-fragmentation cooling crystallization (Wu et al., 2026). To estimate true melt composition at eruption, only EMPA of microlite-poor (<5 vol %) glass is used here.

4.2. Tephra whole-rock compositions

Individual lapilli particles and combined ash samples from the 2022 eruption show andesitic whole-rock compositions, within the compositional range of >1.6 ka edifice-forming lavas from Hunga Tonga and Hunga Ha'apai (55.2–61.8 wt% SiO_2, 2.4–5.2 wt% MgO, and 7.3–11.3 wt% CaO; Figs. 4 and 5; Brenna et al., 2022). The 2022 pyroclastics are overall less evolved and more compositionally diverse (56.5–59.1 wt% SiO_2, 3.3–4.4 wt% MgO, and 8.7–10.1 wt% CaO) than lapilli and bombs erupted in 2009 and 2014–2015 (58.7–59.2 wt% SiO_2, 3.4–3.6 wt% MgO, and 8.7–8.9 wt% CaO), as well as the ~1040–1180 CE caldera-forming pyroclastic deposits (59.1–60.6 wt% SiO_2, 2.7–3.8 wt% MgO, and 7.9–8.9 wt% CaO).

Within the 2021–2022 pyroclastic suite, Stage 1 Surtseyan bombs (erupted during 29–30 December 2021) are the most evolved and overlap with compositions erupted in 2009 and 2014–2015. From Stage 2 onward, compositions are mainly less evolved (Fig. 4), with minor fractions that resemble Stage 1 materials. The overall suite plotted against MgO shows a negative trend in SiO_2, FeO (total iron as FeO), K_2O, TiO_2, and CaO/Al_2O_3, forming a consistent compositional array with the 2009 and 2014–2015 rocks and a subgroup of the pre-~1.6 ka lavas (Figs. 5 and S1). An exception to this are a subset of Stage 3 samples (first lapilli fall on 15 January 2022) with MgO between 3.8 and 4.3 wt% that show a positive trend between K_2O and MgO but no trend in FeO, CaO, SiO_2, and CaO/Al_2O_3 against MgO, which mimics trends in a subset of older lavas (Fig. 5c).

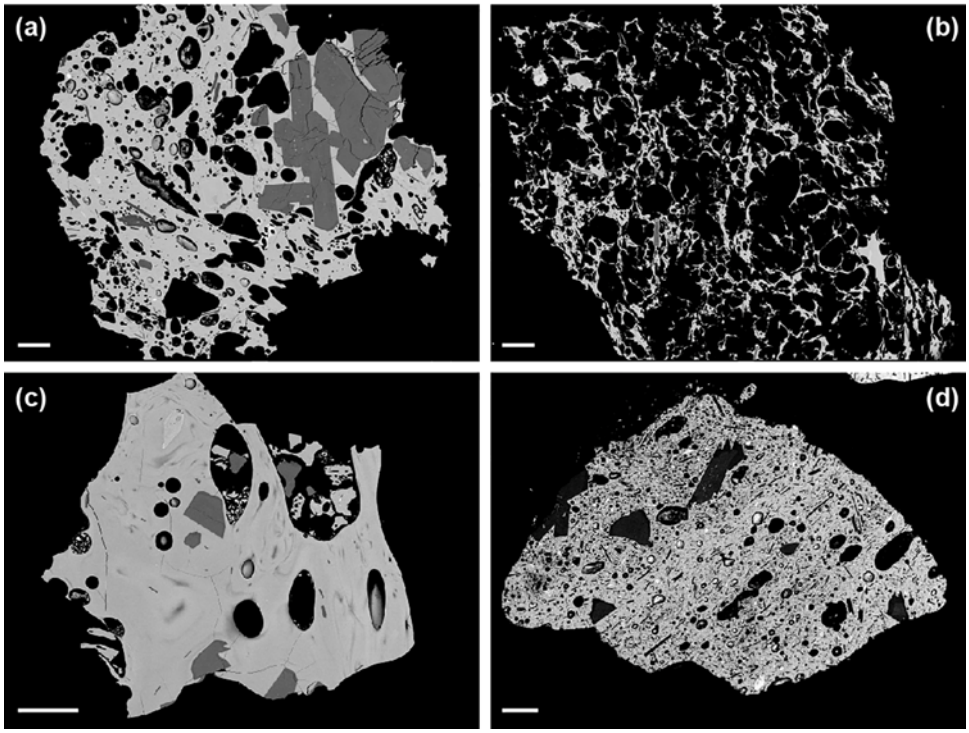

Fig. 3. Backscattered electron (BSE) images of 2022 Hunga tephra. (a) Microlite-poor dark pumice (HT10 from Stage 3) with moderate vesicle proportions and an inclusion of crystal-rich vesicle-free magma. (b) Microlite-poor light pumice (HT10) with extensive vesicles. (c) Microlite-poor dense blocky glass (HT129A from Stage 4) with few vesicles, also showing swirly texture with compositionally more evolved dark bands. (d) Microlite-rich glass (HT10). Scale bar represents 200 μm.

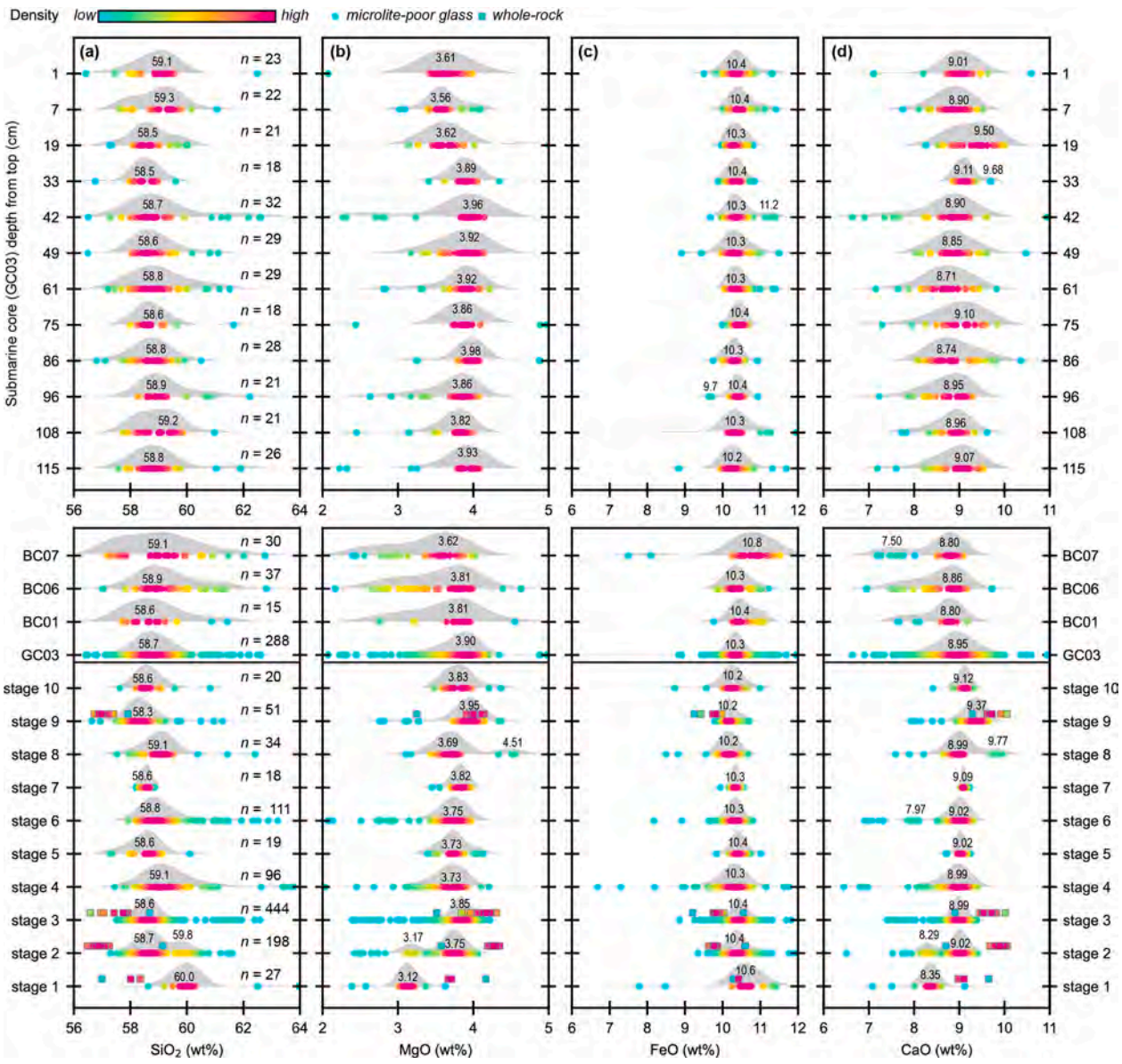

Fig. 4. Major element compositional variations in Hunga microlite-poor glass across the whole 2021–2022 eruptive sequence with whole-rock data plotted for comparison. (a) SiO_2. (b) MgO. (c) FeO. (d) CaO. The top panels show compositional variations along a ~1.2 m submarine gravity core (GC03).

4.3. Microlite-poor tephra glass compositions

Glass from the 2022 eruptive sequence extends to more evolved compositions than whole-rock, with 56.6–65.6 wt% SiO_2, 1.7–5.0 wt% MgO, and 6.4–10.4 wt% CaO (Figs. 4 and 5). The Stage 1 glass is the most evolved, with the highest SiO_2 mode (60.0 wt%) and the lowest MgO (3.1 wt%) and CaO (8.4 wt%) modes in Kernel Density Estimation (KDE) curves (Fig. 4), as well as the lowest S and H_2O contents (Wu et al., 2025). The Stage 2 sample shows bimodal distributions in those elements, with one mode similar to Stage 1 (59.8 wt% SiO_2, 3.2 wt% MgO, and 8.3 wt% CaO) and the other less evolved (58.7 wt% SiO_2, 3.8 wt% MgO, and 9.0 wt% CaO). The less-evolved mode dominates the compositions of the climactic 15 January 2022 eruption (Stages 3–9) and its waning phases (Stage 10), which show little compositional variation (mode at 58.3–59.1 wt% SiO_2, 3.7–4.0 wt% MgO, and 9.0–9.4 wt% CaO). The FeO mode is largely homogenous for all stages (10.2–10.6 wt%). The K_2O mode is the highest (0.6 wt%) in Stage 1, and decreases to ~0.5 wt% during Stages 2–10.

Within the broadly homogenous glass compositions of the climactic phase of the Hunga eruption (Stages 3–10), subtle compositional variation patterns occur. Glass compositions are invariant from Stages 3 to 7, showing only a 0.5 wt% range in SiO_2 modes (58.6–59.1 wt%) and ca. 0.1 wt% range in MgO (3.7–3.9 wt%) and CaO (9.0–9.1 wt%) modes. Stage 8 is dominated by similar compositions, with a sub-population showing the least-evolved glass recorded in the eruption (mode at 4.5 wt% MgO and 9.8 wt% CaO). Stage 9 shows an overall shift to less-evolved compositions and has a single mode of composition intermediate between the two sub-populations present in Stage 8 (mode 4.0 wt% MgO and 9.4 wt% CaO). The waning Stage 10 composition lies between that of Stage 9, and the bulk of the eruption (Stages 3–8).

Submarine Gravity Core (GC03) and Box Core (BC01, 06, and 07) overlap with Stages 3–9 composition (Fig. 4). In the 119 cm-long GC03, compositional modes are 58.5–59.3 wt% SiO_2, 3.6–4.0 wt% MgO, 10.2–10.4 wt% FeO, 8.7–9.5 wt% CaO, and ca. 0.6 CaO/Al_2O_3. From base to top, there is an increase in CaO wt% mode accompanied by a slight decrease in SiO_2 at 33–19 cm above the core base. This may correlate with a shift to less-evolved compositions during Stages 8 and 9, although MgO concentrations are lower than the airfall equivalents.

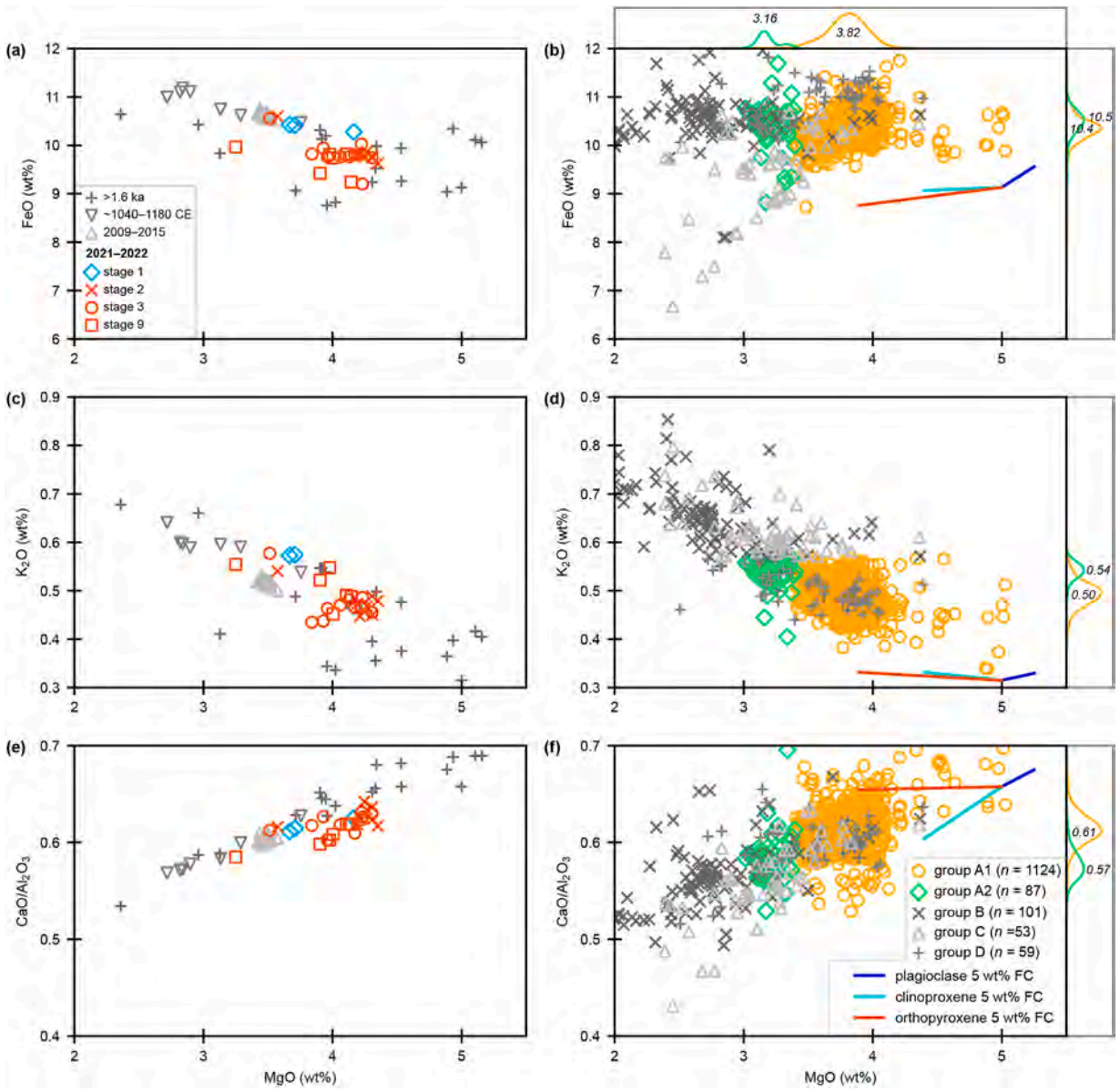

Fig. 5. Major elements plotted against MgO for Hunga whole-rock (left) and microlite-poor glass (right). (a) Whole-rock FeO. (b) Glass FeO. (c) Whole-rock K_2O. (d) Glass K_2O. (e) Whole-rock CaO/Al_2O_3. (f) Glass CaO/Al_2O_3. Kernel density estimation (KDE) curves of major elements in Groups A1 and A2 glasses are shown with the modes labelled.

Across the subaerial and submarine sample suite, internal variation in glass compositions indicate that as the melt evolved towards lower MgO, CaO and CaO/Al_2O_3, SiO_2, TiO_2, and K_2O increased, while K_2O/TiO_2 and FeO remained almost unchanged (Figs. 5 and S1). Based on TiO_2 and K_2O concentrations, glass from the whole Hunga eruptive sequence can be separated into four groups (Figs. 5 and S2 and Table S5), including: (A) low-Ti, low-K; (B) high-Ti, high-K; (C) low-Ti, high-K; and (D) high-Ti, low-K. Group A also has high-Mg (A1) and low-Mg (A2) sub-populations. Group A1 shows the highest MgO, CaO, and CaO/Al_2O_3, and the lowest SiO_2 content, representing the least-evolved compositional group, and is the dominant glass population in Stages 2–10. Group A2 is slightly more evolved with less H_2O and S contents and is only present in Stages 1 and 2. Groups B and C are more evolved with higher SiO_2, and lower MgO and CaO/Al_2O_3. Group B has high FeO comparable to A1 and A2, and is present in Stages 2–4, 6, and 9. Group C shows low FeO and occurs mainly in Stages 1–6. Group D is uncommon and mainly found in submarine cores.

Trace element compositions are overall homogenous across the entire main eruptive Stages 3–10, and Stages 1 and 2 samples show slightly higher concentrations of incompatible elements (details see supplementary text and Figs. S3 and S4 in Appendix A), and are thus not used for further discussion of magma plumbing and eruption dynamics.

4.4. Mineral compositions

Clinopyroxene is present in 2022 Hunga products as green-yellow phenocrysts and microlites with both normal and reverse zoning. Phenocrysts are augite, while microlites are pigeonite. Crystal core compositions are Mg-rich with Mg# mainly between 74 and 88 [Mg# = molar Mg / (Mg + Fe) × 100]. Rims are compositionally more variable with Mg# mainly between 68 and 76 (Fig. 6a). Orthopyroxene phenocrysts are pale-brown and show both normal and reverse zoning. Phenocryst core Mg# varies mainly from 66 to 83, and rim from 65 to 75 (Fig. 6b). Plagioclase phenocrysts are euhedral and commonly normally zoned, with a calcic core [An#88–94, An# = molar Ca / (Ca + Na + K) × 100]. Rim compositions show An# from 76 to 86 (Fig. 6c), with the

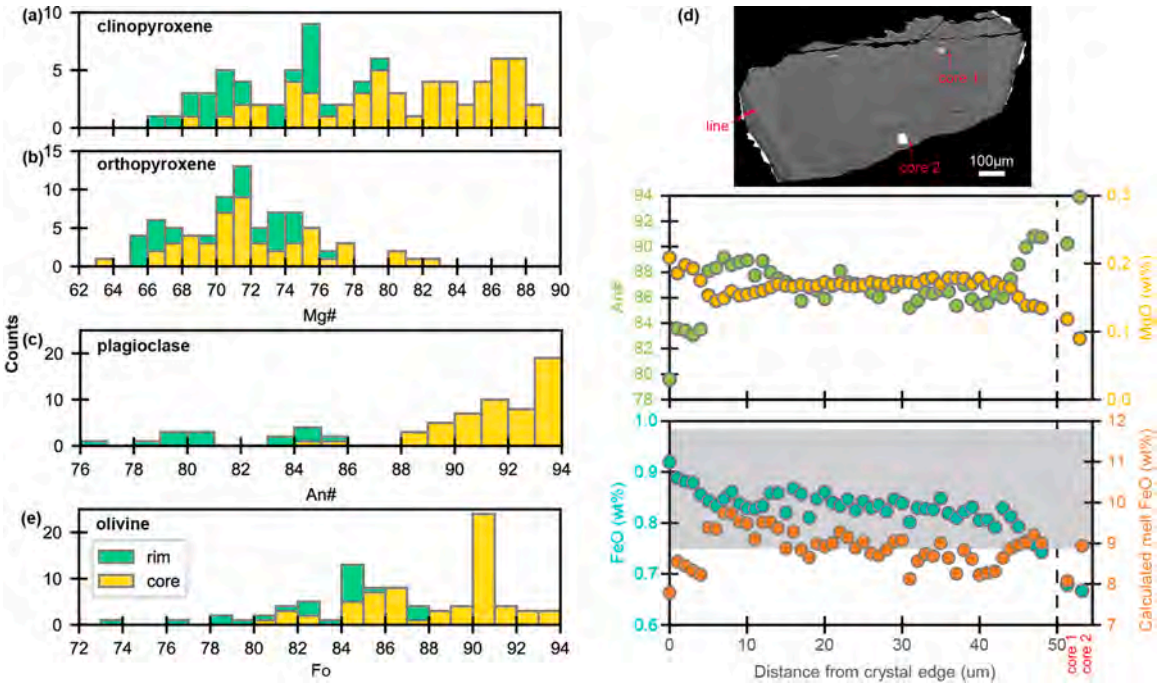

Fig. 6. 2022 Hunga mineral compositions. (a) Histogram of clinopyroxene Mg# ($n = 87$). (b) Histogram of orthopyroxene Mg# ($n = 82$). (c) Histogram of plagioclase An# ($n = 87$). (d) plagioclase core to rim profile showing variations of An#, MgO and FeO as well as calculated melt FeO in equilibrium with plagioclase, with matrix glass FeO range for the same sample (HT10) shown in grey shaded area. (e) Histogram of olivine Fo ($n = 91$).

lowest An# similar to plagioclase microlites. In normally zoned plagioclase phenocrysts, a rim-ward decrease in An# is coupled with an increase in MgO and FeO (Fig. 6d). Plagioclase and pyroxene are the dominant minerals in the 2022 Hunga suite. However, a distinct feature of these eruptive products compared to Hunga samples from previous eruptions (cf., Brenna et al., 2022) is the presence of very rare euhedral olivine crystals up to ~1 mm in diameter. Olivine has high forsterite [Fo = molar Mg / (Mg + Fe) × 100, mainly 84–94] and CaO (0.13–0.29 wt %) contents (Fig. 6e) and contains inclusions of oxides and volatile-rich glass. Olivine rims generally have lower Fo (down to ~73).

5. Discussion

5.1. Magma differentiation

The whole-rock compositions of the 2022 tephra plot along the known Hunga differentiation path (Fig. 5). They can be modelled as products of fractional crystallization of observed phenocryst phases (plagioclase, clinopyroxene, and orthopyroxene) from the most primitive sampled lavas (Fig. 5; Brenna et al., 2022). Mass balance calculations (Stormer Jr and Nicholls, 1978; Petrelli et al., 2005) show that the most evolved 2022 whole-rock compositions (i.e., MgO = 3.57 wt%, sample HT103B from Stage 2) can be produced by fractional crystallization of 21.3 wt% plagioclase, 8.8 wt% clinopyroxene, and 4.4 wt% orthopyroxene from the primitive magma [i.e., MgO = 5 wt%, sample HH78 from Brenna et al. (2022); Table S6]. Additional evolutionary sub-trends observed within the 2022 compositions include both K_2O enrichment and depletion during differentiation (e.g., decreasing MgO). Since potassium is incompatible in the observed phenocryst assemblage, it should become enriched in the melt during fractional crystallization. Thus, the linear K_2O depletion trend can only result from eruption of magma increasingly mixed with a less-evolved component. Considering a slight compositional heterogeneity (e.g., TiO_2, FeO, K_2O, and CaO) observed in the most primitive lava samples, different melt pockets with individual fractionating assemblages were likely mixed.

Microlite-poor glass shows a larger compositional scatter than whole-rock samples reflecting melt heterogeneity at micron-scale, while whole-rock analysis is buffered by a much larger sample size and the crystal cargo (Ubide et al., 2022). Also, the glass dataset samples a wider diversity of particles from the eruption than the whole-rock set (1424 vs 28 analyses). The dominant glass group (A1) comprises a single main population (Fig. 5), consistent with crystallization of 18.8 wt% plagioclase, 8.3 wt% clinopyroxene, and 3.8 wt% orthopyroxene from sample HH78 (Fig. 5; Table S6). This relatively small amount of plagioclase crystallization is consistent with a weak negative Eu anomaly, and Sr behaving almost incompatibly in the groundmass glass (Figs. S3 and S4). The glass data variability can result from crystalizing differing amounts of the same minerals from slightly compositionally variable magma, reflected by the whole-rock ranges. Overall, two main crystallization trends are observed: (1) a Fe-constant trend from group A1 through A2 to B; and (2) a Fe-depletion trend from group A (A1/A2) to C. The Fe-constant trend is broadly consistent with the Hunga whole-rock compositional array, thus represents melts produced by crystallization of the observed phenocryst assemblage. Since all the tephra samples analyzed are phenocryst- and microlite-poor, glass compositional differences likely reflect different melt compositions in the storage zone. Group A2 glass is dominant in the pre-climax eruption Stage 1. Compared to group A1, A2 glass is more evolved with a narrower compositional range, which can be produced from A1 by slightly more crystallization of the same phenocryst assemblage (5.3 wt% plagioclase, 3.4 wt% clinopyroxene, and 1.5 wt% orthopyroxene; Table S6). From pre-climax eruptions (Stages 1 and some of Stage 2 particles) to the climactic 15 January 2022 event (Stages 3–10), the shift of dominant glass compositions from group A2 to A1 is consistent with erupting more-primitive whole-rock compositions. The shift corresponds to higher magma volatile (H_2O and S) concentrations (Wu et al., 2025) and higher magma pressure/depth based on the experimentally-determined clinopyroxene-plagioclase cotectics (Fig. 7; Firth et al., 2019). This suggests that groups A1 and A2 represent two separate magmas. Group C glass has lower FeO, CaO, and CaO/Al_2O_3, as well as higher SiO_2 and K_2O/TiO_2. Thus compared to the Fe-constant trend, the Fe-depletion trend likely results from fractionation of more clinopyroxene and

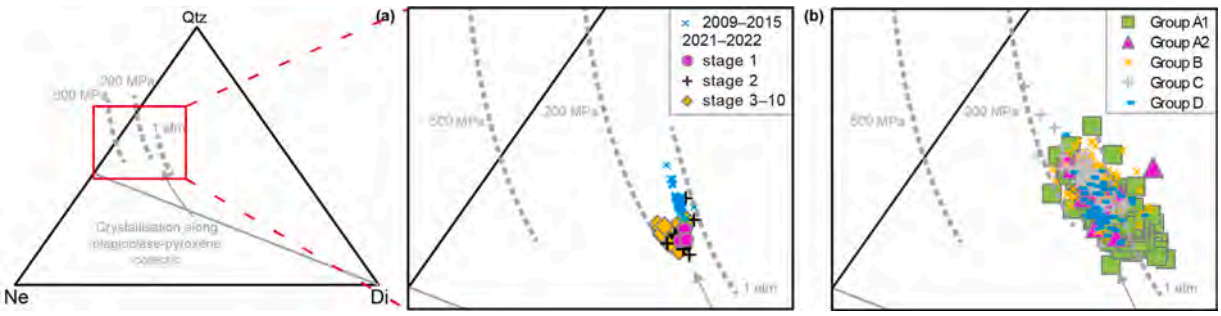

Fig. 7. Quartz (Qtz)-nepheline (Ne)-diopside (Di) ternary diagram showing Hunga magma compositions against experimentally-determined plagioclase-pyroxene cotectics (Firth et al., 2019). (a) whole-rock. (b) microlite-poor glass.

magnetite (a rare phase in Hunga magma) in the mineral assemblage, potentially reflecting different magma storage and/or degassing histories.

Mingling of magma represented by dominantly group A compositions with minor group C is frequently recorded in individual shards, expressed as micron-scale swirled textures visible in backscatter electron images (Fig. 2c). The swirly texture and preservation of the chemical contrasts suggest mingling of heterogeneous magma occurred shortly prior to chilling, during the eruption (cf., González-García et al., 2023). This is consistent with timescales of minutes derived from the modelling of water diffusion in Hunga glass (Wu et al., 2025).

5.2. Pre-eruptive magma decompression

The 15 January 2022 Hunga minerals are characterized by unusually primitive compositions, including Mg-rich olivine (Fo>90) and clinopyroxene (Mg# up to 89), as well as Ca-rich plagioclase (An#>88). Hunga olivine is CaO-rich (>0.15 wt%) and all mineral phases contain abundant co-magmatic melt inclusions, with compositions suggesting that olivine and clinopyroxene crystals were cogenetic with Hunga magmas (Wu et al., 2025). The high MgO/FeO ratios in both minerals are consistent with their more-primitive melt inclusion compositions and may result from oxidized magma conditions, where a significant part of iron is present as Fe^{3+}, which is less favored in olivine and pyroxene crystal lattices than Fe^{2+} (Wu et al., 2025).

The Ca-rich plagioclase in Hunga rocks is interpreted to indicate high magma water content (Brenna et al., 2022). Both plagioclase and clinopyroxene show normal zonation with overgrowth rims characterized by lower Ca and Mg contents, respectively. This indicates changes in host magma compositions before eruption. The final host magma was either (1) compositionally more evolved, and/or (2) more water-degassed. We exclude scenario (1) because Hunga glass compositional ranges are narrow. Melt inclusions in plagioclase have similar compositions to the host glass (Wu et al., 2025). Even though Ca-poor plagioclase rims show higher FeO and MgO compared to the Ca-rich core (Fig. 6), estimated melt FeO in equilibrium with Hunga plagioclase rims at 1050 °C is similar to or slightly higher than the core [following Bindeman et al. (1998)]. Thus, melt dehydration led to growth of Ca-poor plagioclase rims. An# positively correlates with magma temperature and water content (Putirka, 2005; Lange et al., 2009). Based on Lange et al. (2009) a decrease of 5 and 10 in An# requires a melt-water reduction of 0.9 and 1.5 wt%, respectively, assuming a constant melt composition and temperature. If magma cools, less water exsolution is needed. Wu et al. (2025) measured a maximum water content in plagioclase melt inclusions of 4.6 wt%, with concentrations of ~3 wt% H_2O to near zero in groundmass glass. Notably, Wu et al. (2025) observed two coexisting glass types with similar major element compositions, but different water contents. The water-rich glass (2.3 wt% H_2O) was vesicle-free, and the water-poor glass (1.3 wt%) was vesicle-rich, representing different degrees of melt water exsolution.

Collectively the petrological results shows that the core-rim compositional change in plagioclase phenocrysts resulted from a major decompression event immediately preceding the explosive eruption. The accompanying vesicle growth likely built high gas-overpressures that could explain the major transition of the eruption to extreme explosivity on 15 January 2022.

5.3. Hunga magma reservoir

The 2022 Hunga tephra compositions suggest the presence of two main magmas (A1 and A2), along with minor sub-batches (B, C, and D). The more evolved A2 magma is similar to the 2009 and 2014–2015 whole-rock compositions. It was only erupted in Stages 1 and 2, suggesting that the pre-climax eruptions tapped a relict 2009–2015 reservoir, or that it was a similar magma stored under similar conditions to the earlier events. Geophysical data suggest two magma reservoirs were tapped during the eruption (Le Mével et al., 2023); the main reservoir beneath the caldera at depth of 2–6 km and other reservoirs, extending up to 10 km-depth, consistent with new experimental results (Califano et al., 2026). The magma depth estimate from magma volatile saturation is 2.1 to >5.6 km (Wu et al., 2025). From Stage 3 onward, the dominant A1 composition erupted on 15 January 2022 was more primitive than earlier-erupted magma compositions. This was likely hosted in the deeper part of the main reservoir or possibly the other deeper reservoirs suggested by Le Mével et al. (2023). Crystals from Stage 3 (HT10) host melt inclusions with variable water contents that indicate a variety of entrapment depths if they did not lose water during pre-eruptive transportation. This implies that the climactic eruption tapped a cross-section through the depth of the main and/or offset reservoirs.

The homogeneity of 2022 A2 glass and corresponding whole-rock compositions along with the 2009 and 2014–2015 compositions, indicate a well-mixed shallow magma reservoir as proposed by Brenna et al. (2022). The more primitive A1 compositions show a greater variation around a central cluster (Fig. 5), which suggests it is weakly compositionally zoned. The compositional gap between A1 and A2 suggests that the two magma bodies were separate pockets before eruption (Fig. 8). The minor glass groups (B, C, and D) represent mixing of smaller or isolated melt lenses that were mixed into the main magma batches during eruption. Magma mixing during the eruption is also supported by whole-rock K_2O variations across the main stages.

5.4. Top-down or bottom-up eruption triggering?

Major explosive eruptions from mafic-intermediate volcanoes are often associated with the rapid intrusion of fresh, gas-rich and often more primitive magmas into a magmatic system (e.g., Sparks et al., 1977; Pallister et al., 1992; Morgavi et al., 2017). In the Hunga case, gas-rich and more primitive A1 compositions likely drove the Hunga climactic eruption. Less clear, however, is when did this magma arrive? We discuss two scenarios below: (1) A1 magma was resident for at least a few decades; or (2) it arrived on 13 January 2022 to cause a sudden increase in eruption magnitude. Scenario 1 could be an argument for

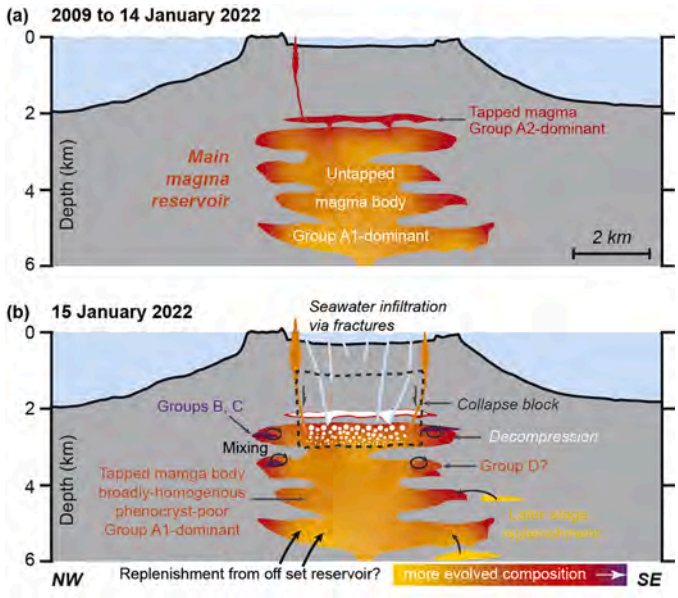

Fig. 8. Conceptual model showing the processes leading to the 2022 Hunga eruption. (a) Eruptions between 2009 and 14 Janurary 2022 only tapped a shallow magma body at the top of the main reservoir. (b) After the immediate pre-climax eruption on 14 January 2022, the shallow magma body was largely exhausted. The resulting decompression of the deeper magma body along with seawater infiltration through new fractures led to a series of smaller eruptions overnight before the 15 January 2022 climactic event.

top-down decompression-driven eruption triggering, while scenario 2 could indicate a recharge driver.

Surtseyan eruption episodes from Hunga in the weeks leading up to the climactic 15 January 2022 eruption represent precursors. The Stages 1 and 2 eruptions between 19 December 2021 and 14 January 2022 (Fig. 2) were similar to the 2009 and 2014–2015 events in eruptive style and pattern and were fed by a similar magma reservoir. We compare the eruption magnitudes below. The 2009 eruption volume was ~ 0.0176 km^3 (Vaughan and Webley, 2010), mainly erupted over 3–5 days, indicating an average volumetric eruption rate (VER) of ~70 m^3/s (assuming 3 days). The 2014–2015 eruption produced at least 0.0479 km^3, over 3 weeks (Garvin et al., 2018), however, for much of this time, the volcano was quiescent. Most volume was erupted during five pulses, each ~24–48 h-long, suggesting an average VER of 115 m^3/s.

The 2021–2022 cycle was similar to earlier ones with long pauses interrupted by vigourous eruptive pulses, especially during 19–21 December 2021, 27–30 December 2021, and 13–14 January 2022. The December 2021 eruptions had a similar VER to 2009–2015 events based on similar plume heights, eruption jet heights and base-surge runouts (the latter ~1 km radius). Scaling these geometrically for the 13–14 January 2022 eruption (base surges of ~2.5 km radius) suggests an average VER of at least six times greater at ~700 m^3/s. Videos and photographs show that most of the 13–14 January 2022 plume was formed by steam, buoyantly rising isolated jets and base surges, i.e., a continuous eruption had not started yet. If we assume a VER of 700 m^3/s over ~16 h of seismic activity, the 13–14 January 2022 event erupted ~0.04 km^3, similar to the entire 2014–2015 episode.

Despite the 13–14 January 2022 eruption being larger in magnitude than any seen in the historical record at Hunga, it did not show a radical change in volcanic style to the past events. Its VER was four orders of magnitude lower than during the peak of the 15 January event (1.3–2.3 $\times 10^6$ m^3/s; Suzuki et al., 2025). Considering the total eruptive volume estimated by caldera displacement (~6.85 km^3; Ribó et al., in review), the average VER over the 11 hour event was 1.7 $\times 10^5$ m^3/s, three orders of magnitude greater than the 13–14 January 2022 event.

The A1 compositions were first erupted from 13 January 2022 (within Stage 2), or during the rapid accelerating phase of the climactic event (Stage 3). This is a more primitive composition than seen before at Hunga and was either absent in 2009, 2014–2015 and 19–30 December 2021, or it was not tapped by these events. Evidence presented here suggests that interaction of A1 magma with degassed resident magma was brief and syn-eruptive. A1 magma contains low crystal contents with little textural evidence for long-lived disequilibrium and plagioclase rim zonation evidences sudden decompression before eruption.

A bottom-up eruption driver is supported by the first appearance of A1 magma only after 13 January 2022. This suggests that the shallow magma lens that fed 2009–2021 events was exhausted and A1 magma replaced it, causing vesiculation and eruption. The 15 January 2022 climactic event began with ~15 min of initial eruptions similar to those during previous days to weeks, but after two sets of seismically-recorded explosions, the VER transformed markedly (Van Eaton et al., 2023; Mastin et al., 2024). The explosions likely represent magma seawater interaction, but the major increase in eruption rate was likely due to the rapid rise and expansion of gas-rich A1 magma.

As an alternative, a top-down eruption triggering model could also be possible, although a deep-mafic recharge can be ruled out. Evidence for A1 magma being resident for decades is the minor chemical difference between A1 and A2 melts; explainable by only a few percent crystallization of the phenocrystic phases. Glass and whole-rock compositions of 2009–2022 products form a generally continuous spectrum that is considerably more evolved than more ancient mafic products of Hunga. Additionally, the volatile composition and estimated pressures from melt inclusions in all phenocryst phases of 2021–2022 eruptives (Wu et al., 2025), are consistent with the same shallow reservoir estimated for historic eruptives (Brenna et al., 2022). While caldera collapse of 6.85 km^3 occurred, this volume of A1 magma could readily have derived from the pre-eruption ~27 km^3 magma reservoir (Le Mével et al., 2023).

Why did the A1 magma not appear until 13–14 January 2022? Perhaps the rate and depth of magma extraction and depressurization was not high enough. Only from 13 to 14 January 2022 did VER exceed the largest 2009–2021 eruptions by around an order of magnitude for ~16 h. This was enough to depressurize and destabilize deep into the magmatic system to trigger the movement and vesiculation of a previously isolated gas-rich magma (A1). Collapse of the vent below sea-level early on 13 January 2022 shows that deep-fracturing and dilation had already started on the caldera ring-fault system, causing depressurization (similar to edifice unloading, e.g., Alidibirov and Dingwell, 1996). Under these conditions, penetration of seawater into the edifice and intense phreatomagmatism is likely (e.g., Self and Sparks, 1978). During and following the 13–14 January eruptive pulse, regular small scale tsunami (±15 cm waves) occurred until <6 h before the climactic eruption started (Borrero et al., 2023). This suggests that there was ongoing submarine volcanism and penetration of sea-water into the upper magmatic system until shortly before the climactic event.

Based on current evidence it appears that both top-down and bottom up mechanisms were responsible for triggering the 15 January 2022 Hunga eruption. Despite the lack of an obvious deep mafic magma "recharge" trigger as seen in other systems (e.g., Firth et al., 2015), the Hunga 2022 climactic eruption was driven by a resident, but previously isolated, gas-rich magma, augmented by rapid depressurization and runaway phreatomamatism as the caldera faults re-activated and seawater penetrated deeply into the magma system.

5.5. Correlating compositional changes with eruption dynamics

With eye-witness and geophysical recording of the eruption, major eruptive phases can be timed via the arrival of tsunami waves and deposits (Fig. 1). Tsunamis during Stage 3 (04:10–04:18 and 04:25–04:35 UTC) and between Stages 4 and 5 (05:05–05:15) were 2–6 m runup and generated by large submarine explosions (Purkis et al., 2023). These were followed by the peak tsunami (>18 m at 05:45), initiated by

caldera collapse at 05:30 (Cronin et al.). Another moderate tsunami (<3 m) between Stages 8 and 9 (at 08:45–09:00), was likely triggered by an explosive blast at 08:30 (Tarumi and Yoshizawa, 2023; Van Eaton et al., 2023).

To relate the tephra fall sequence to the eruption dynamics, we must consider the lag between vent processes and deposition of tephra at sampling sites 70–100 km distant. Based on eyewitness observations, the lag between the suddenly rising eruption plume (from 04:15), to the first lapilli fall was ~30–40 min. Tsunami travel times for 60–80 km distances (assuming deep water and narrow coastal margins) are ~8–12 min with wave trains lasting tens of minutes (Borrero et al., 2023). Therefore, fall deposits may lag ~10–20 min from the tsunami arrival. The early explosions (04:15–04:25) were likely driven by intense phreatomagmatism as seawater penetrated re-activated ring-fault systems to encounter magma. The eruption of water-rich magma (Wu et al., 2025), corresponds also to the peak intensity of the eruption from ~04:25 to ~5:00 (Mastin et al., 2024). Bulk compositions through Stages 3–7 are uniform and there was little compositional change of fall deposits formed before and after the caldera-collapse induced peak tsunami (Stages 5 and 6). A shift to less-evolved compositions occurred in Stages 8 and 9 (Fig. 4), after renewed explosions at the volcano. This likely records the supply of slightly more-primitive magma in zones previously untapped, possibly erupted through ring-fault vents activated by caldera collapse.

6. Conclusions and implications

Time-resolved sampling of the 2022 Hunga eruption allows a high-resolution examination of magmatic-volcanic processes leading up to and during the ~11 h caldera-forming event on 15 January 2022. Surtseyan eruptions during the early weeks of the 2021–2022 episode erupted similar evolved compositions with similar processes and magnitudes to the 2009 and 2004–2015 events. This suggests that the 2021–2022 Hunga eruption cycle began by tapping a resident shallow magma lens (A2 magma) that had fueled the previous events.

A major change in eruption magnitude, coupled with the first appearance of a slightly more-primitive magma (A1) occurred from 13 January 2022. This suggests that the gas-rich A1 magma entered the shallow magmatic system and began vesiculating. From this point, the volcanic and magmatic system was set on a pathway to destabilization. Over 16 h of high eruption rates, deep decompression caused vent foundering below sea-level, caldera fault re-activation and magma vesiculation. This was accompanied by regular pulsing small-tsunami seen until 6 h before the climactic event.

The following climactic 15 January 2022 eruption was driven by high rates of eruption of magma with high water content (mode at 0.89–1.75 wt% for Stages 3–10 vs 0.47–0.55 wt% for Stages 1 and 2; Wu et al., 2025), along with seawater ingress and runaway phreatomagmatic explosions. The lack of distinct mafic glass, the low phenocryst content and the absence of disequilibrium textures or reverse zonation at phenocryst rims indicate the Hunga eruption was not triggered by a sudden deep mafic magma recharge. Instead, normally zoned plagioclase phenocrysts with Ca-poor but Mg- and Fe-rich rims evidence a major decompression event within a resident gas-rich magma before 13 January 2022.

In many long-lived volcanic systems, caldera-forming eruptions follow thermal maturation of the crust primed by pre-caldera magmatism, thereby promoting magma evolution over time. At Hunga, this priming could be evidenced during the ~1040–1180 CE caldera-forming cycle, where the caldera-forming eruption produced more evolved magmas (59.1–60.6 wt% SiO_2 and 2.7–3.8 wt% MgO), than most primitive lavas in the older edifice (55.2–61.8 wt% SiO_2 and 2.4–5.2 wt % MgO; Brenna et al., 2022). However, the 2009–2015 eruptions were slightly less evolved (58.7–59.2 SiO_2 and 3.4–3.6 wt% MgO), and the climactic 2022 caldera-forming eruption was even more primitive (56.5–59.1 wt% SiO_2 and 3.3–4.4 wt% MgO). This could be explained by a successive lowering of the central Hunga edifice by repeated caldera collapses, which also led to fracturing and weakening of the crust below. The lower edifice load and ring-fault fractures may have limited the capacity to hold the same magma reservoir growth pressures as ~1000 years before. Thus, more primitive, water-rich and phenocryst-poor magmas erupted in 2022. This model could explain activity rates at other basaltic to andesitic volcanoes with frequently repeated caldera-forming explosive eruptions.

CRediT authorship contribution statement

Jie Wu: Writing – review & editing, Writing – original draft, Visualization, Validation, Methodology, Investigation, Formal analysis, Data curation, Conceptualization. **Shane J. Cronin:** Writing – review & editing, Writing – original draft, Visualization, Validation, Supervision, Resources, Project administration, Methodology, Investigation, Funding acquisition, Formal analysis, Data curation, Conceptualization. **Marco Brenna:** Writing – review & editing, Writing – original draft, Supervision, Project administration, Methodology, Investigation, Funding acquisition, Formal analysis, Conceptualization. **Joali Paredes-Mariño:** Writing – review & editing, Data curation. **Sung-Hyun Park:** Writing – review & editing, Resources, Funding acquisition. **Mila Huebsch:** Writing – review & editing, Data curation. **Alessio Pontesilli:** Writing – review & editing. **Chris Firth:** Writing – review & editing. **David Adams:** Writing – review & editing, Data curation. **Teresa Ubide:** Writing – review & editing, Data curation. **Kyle Hamilton:** Writing – review & editing, Data curation. **Alice MacDonald:** Writing – review & editing, Data curation. **Enrico Califano:** Writing – review & editing. **James D.L. White:** Writing – review & editing. **Terry Plank:** Writing – review & editing. **Marta Ribó:** Writing – review & editing. **Ingrid Ukstins:** Writing – review & editing, Data curation. **Frank Ramos:** Writing – review & editing. **Silvio Mollo:** Writing – review & editing. **Jihyuk Kim:** Writing – review & editing, Resources. **Folauhola Latu'ila:** Writing – review & editing, Resources. **Taaniela Kula:** Writing – review & editing, Resources. **Renne Vaiomounga:** Writing – review & editing, Resources.

Declaration of competing interest

Authors declare that they have no competing interests.

Acknowledgments

We thank Stuart Morrow for support during LA-ICP-MS analyses. This work was supported by Royal Society of New Zealand Te Apārangi Marsden Fund (MFP-UOO2218), New Zealand Government Ministry of Business Innovation and Employment Endeavour Research Programmes (UOAX1913, UOA24103, UOA2494), and Korea Polar Research Institute (PE22550). We thank Editor Rosemary Hickey-Vargas for editorial handling and Sebastian Watt and Etienne Médard for their thoughtful reviews.

Supplementary materials

Supplementary material associated with this article can be found, in the online version, at doi:10.1016/j.epsl.2026.120041.

Data availability

All data are available in the main text or the supplementary materials.

References

Alidibirov, M., Dingwell, D.B., 1996. Magma fragmentation by rapid decompression. Nature 380, 146–148. https://doi.org/10.1038/380146a0.

Bindeman, I.N., Davis, A.M., Drake, M.J., 1998. Ion microprobe study of plagioclase-basalt partition experiments at natural concentration levels of trace elements. Geochim. Cosmochim. Acta 62, 1175–1193. https://doi.org/10.1016/S0016-7037(98)00047-7.

Borrero, J.C., Cronin, S.J., Latu'ila, F.H., Tukuafu, P., Heni, N., Tupou, A.M., Kula, T., Fa'anunu, O., Bosserelle, C., Lane, E., 2023. Tsunami runup and inundation in Tonga from the January 2022 eruption of Hunga Volcano. Pure Appl. Geophy. 180, 1–22. https://doi.org/10.1007/s00024-022-03215-5.

Brenna, M., Cronin, S.J., Smith, I.E., Pontesilli, A., Tost, M., Barker, S., Tonga'onevai, S., Kula, T., Vaiomounga, R., 2022. Post-caldera volcanism reveals shallow priming of an intra-ocean arc andesitic caldera: hunga volcano, Tonga, SW Pacific. Lithos 412, 106614. https://doi.org/10.1016/j.lithos.2022.106614.

Bryan, W.B., Stice, G.D., Ewart, A., 1972. Geology, petrography, and geochemistry of the volcanic islands of Tonga. J. Geophys. Res. 77, 1566–1585. https://doi.org/10.1029/JB077i008p01566.

Califano, E., Mollo, S., Brenna, M., Pontesilli, A., Wu, J., Marks, P., Eul, D., Nowak, M., Cronin, S.J., Di Fiore, F., Vona, A., Abeykoon, S., Di Genova, D., Romano, C., Scarlato, 2026. Experimental and thermodynamic constraints on the magmatic variables governing pre-eruptive conditions at Hunga volcano: Development of a new equilibrium orthopyroxene-clinopyroxene thermometer. Chem. Geol. 708, 123328. https://doi.org/10.1016/j.chemgeo.2026.123328.

Carn, S.A., Krotkov, N.A., Fisher, B.L., Li, C., 2022. Out of the blue: volcanic SO_2 emissions during the 2021–2022 eruptions of Hunga Tonga—Hunga Ha'apai (Tonga). Front. Earth. Sci. 10, 976962. https://doi.org/10.3389/feart.2022.976962.

Caulfield, J.T., Cronin, S.J., Turner, S.P., Cooper, L.B., 2011. Mafic Plinian volcanism and ignimbrite emplacement at Tofua volcano, Tonga. Bull. Volcanol. 73, 1259–1277. https://doi.org/10.1007/s00445-011-0477-9.

Chaknova, M., Giachetti, T., Paredes-Mariño, J., Soule, A., Van Eaton, A.R., Beinart, R., Crundwell, M., Cronin, S.J., Jutzeler, M., Fauria, K.E., 2025. How did westward volcaniclastic deposits accumulate in the deep sea following the January 2022 eruption of Hunga Volcano? Geochem. Geophys. Geosyst. 26. https://doi.org/10.1029/2024GC011629 e2024GC011629.

Clare, M.A., Yeo, I.A., Watson, S., Wysoczanski, R., Seabrook, S., Mackay, K., Hunt, J.E., Lane, E., Talling, P.J., Pope, E., Cronin, S., Ribó, M., Kula, T., Tappin, D., Henrys, S., de Ronde, C., Urlaub, M., Kutterolf, S., Fonua, S., Panuve, S., Veverka, D., Rapp, R., Kamalov, V., Williams, M., 2023. Fast and destructive density currents created by ocean-entering volcanic eruptions. Science 381, 1085–1092. https://doi.org/10.1126/science.adi3038.

Colombier, M., Scheu, B., Wadsworth, F.B., Cronin, S., Vasseur, J., Dobson, K.J., Hess, K., Tost, M., Yilmaz, T.I., Cimarelli, C., 2018. Vesiculation and quenching during surtseyan eruptions at Hunga Tonga-Hunga Ha'apai volcano, Tonga. J. Geophys. Res.-Solid Earth 123, 3762–3779. https://doi.org/10.1029/2017JB015357.

Cronin, S., Brenna, M., Smith, I., Barker, S., Tost, M., Ford, M., Tonga'onevai, S., Kula, T., Vaiomounga, R., 2017. New volcanic island unveils explosive past. Eos (Washington DC) 98, 1. https://doi.org/10.1029/2017EO076589.

Cronin, S., Kula, T., Ukstins, I., Ramos, F., Paredes-Marino, J., Park, S., White, J., Baxter, R., Brenna, M., Van Eaton, A., 2023. Extreme explosivity of the 15 January 2022 Hunga eruption, Tonga, driven by magma-mixing, caldera collapse and magma-water interaction. https://hdl.handle.net/10523/43599.

Cronin, S.J., Steinke, B., Borrero, J.C., Okal, E.A., Ribó, M., Wu, J., White, J.D.L., Brenna, M., Paredes-Mariño, J., Huebsch, M., Baxter, R., Speidel, U., van Eaton, A., Mastin, L., Clare, M., Yeo, I.A, Hunt, J.E., Nash, J., Garvin, J.B., Vaiomounga, R., Kula, T., Park, S.-.H., n.d. Delayed submarine caldera subsidence creates extreme tsunami hazard (in review) Sci. Adv.

Firth, C.W., Cronin, S.J., Turner, S.P., Handley, H.K., Gaildry, C., Smith, I., 2015. Dynamics and pre-eruptive conditions of catastrophic, ignimbrite-producing eruptions from the Yenkahe Caldera, Vanuatu. J. Volcanol. Geotherm. Res. 308, 39–60. https://doi.org/10.1016/j.jvolgeores.2015.10.012.

Firth, C., Adam, J., Turner, S., Rushmer, T., Brens, R., Green, T.H., Erdmann, S., O'Neill, H., 2019. Experimental constraints on the differentiation of low-alkali magmas beneath the Tonga arc: implications for the origin of arc tholeiites. Lithos 344, 440–451. https://doi.org/10.1016/j.lithos.2019.07.008.

Garvin, J.B., Slayback, D.A., Ferrini, V., Frawley, J., Giguere, C., Asrar, G.R., Andersen, K., 2018. Monitoring and modeling the rapid evolution of Earth's newest volcanic island: hunga Tonga Hunga Ha'apai (Tonga) using high spatial resolution satellite observations. Geophys. Res. Lett. 45, 3445–3452. https://doi.org/10.1002/2017GL076621.

Gatliff, R.W., Helu, S., Singh, R., 1991. Annual report of the world volcanic eruptions in 1988. Bull. Volcanol. 53, 1–108. https://doi.org/10.1007/BF00305006.

Global Volcanism Program, 2015. Report on Hunga Tonga-Hunga Ha'apai (Tonga). In: Wunderman, R. (Ed.), Bulletin of the Global Volcanism Network 40:1. Smithsonian Institution. https://doi.org/10.5479/si.GVP.BGVN201501-243040.

González-García, D., Boulesteix, T., Klügel, A., Holtz, F., 2023. Bubble-enhanced basanite-tephrite mixing in the early stages of the Cumbre Vieja 2021 eruption, La Palma, Canary Islands. Sci. Rep. 13, 14839. https://doi.org/10.1038/s41598-023-41595-3.

Gupta, A.K., Bennartz, R., Fauria, K.E., Mittal, T., 2022. Eruption chronology of the December 2021 to January 2022 Hunga Tonga-Hunga Ha'apai eruption sequence. Commun. Earth. Environ. 3, 314. https://doi.org/10.1038/s43247-022-00606-3.

Hall, A., Cronin, S., Clark, G., Sear, D., Shane, P., 2025. A new subaerial record of explosive volcanism and tsunami along the Tonga Volcanic Arc, Tonga, SW Pacific. IAVCEI Scientific Assembly 2025, Geneva.

Kelly, L.J., Fauria, K.E., Manga, M., Cronin, S.J., Latu'ila, F.H., Paredes-Mariño, J., Mittal, T., Bennartz, R., 2024. Airfall volume of the 15 January 2022 eruption of Hunga volcano estimated from ocean color changes. Bull. Volcanol. 86, 59. https://doi.org/10.1007/s00445-024-01744-6.

Lange, R.A., Frey, H.M., Hector, J., 2009. A thermodynamic model for the plagioclase-liquid hygrometer/thermometer. Am. Mineral. 94, 494–506. https://doi.org/10.2138/am.2009.3011.

Le Mével, H., Miller, C.A., Ribó, M., Cronin, S., Kula, T., 2023. The magmatic system under Hunga volcano before and after the 15 January 2022 eruption. Sci. Adv. 9, eadh3156. https://doi.org/10.1126/sciadv.adh3156.

Mastin, L.G., Van Eaton, A.R., Cronin, S.J., 2024. Did steam boost the height and growth rate of the giant Hunga eruption plume? Bull. Volcanol. 86, 64. https://doi.org/10.1007/s00445-024-01749-1.

Matoza, R.S., Fee, D., Assink, J.D., Iezzi, A.M., Green, D.N., Kim, K., Toney, L., Lecocq, T., Krishnamoorthy, S., Lalande, J., 2022. Atmospheric waves and global seismoacoustic observations of the January 2022 Hunga eruption, Tonga. Science 377, 95–100. https://doi.org/10.1126/science.abo7063.

Millan, L., Santee, M.L., Lambert, A., Livesey, N.J., Werner, F., Schwartz, M.J., Pumphrey, H.C., Manney, G.L., Wang, Y., Su, H., 2022. The Hunga Tonga-Hunga Ha'apai hydration of the stratosphere. Geophys. Res. Lett. 49. https://doi.org/10.1029/2022GL099381 e2022GL099381.

Morgavi, D., Arienzo, I., Montagna, C., Perugini, D., Dingwell, D.B., et al., 2017. Magma mixing: history and dynamics of an eruption trigger. In: Gottsmann, J., et al. (Eds.), Volcanic Unrest: From Science to Society. Springer, Cham, Switzerland, pp. 123–137. https://doi.org/10.1007/11157_2017_30.

Pérez, W., Freundt, A., 2006. The youngest highly explosive basaltic eruptions from Masaya Caldera (Nicaragua): stratigraphy and hazard assessment. Geol. Soc. Am. Spec. Pap. 412, 189–207. https://doi.org/10.1130/2006.2412(10).

Pallister, J.S., Hoblitt, R.P., Reyes, A.G., 1992. A basalt trigger for the 1991 eruptions of Pinatubo volcano? Nature 356, 426–428. https://doi.org/10.1038/356426a0.

Petrelli, M., Poli, G., Perugini, D., Peccerillo, A., 2005. PetroGraph: a new software to visualize, model, and present geochemical data in igneous petrology. Geochem. Geophys. Geosyst. 6, Q07011. https://doi.org/10.1029/2005GC000932.

Poli, P., Shapiro, N.M., 2022. Rapid characterization of large volcanic eruptions: measuring the impulse of the Hunga Tonga Ha'apai explosion from teleseismic waves. Geophys. Res. Lett. 49. https://doi.org/10.1029/2022GL098123 e2022GL098123.

Proud, S.R., Prata, A.T., Schmauß, S., 2022. The January 2022 eruption of Hunga Tonga-Hunga Ha'apai volcano reached the mesosphere. Science 378, 554–557. https://doi.org/10.1126/science.abo4076.

Purkis, S.J., Ward, S.N., Fitzpatrick, N.M., Garvin, J.B., Slayback, D., Cronin, S.J., Palaseanu-Lovejoy, M., Dempsey, A., 2023. The 2022 Hunga-Tonga megatsunami: near-field simulation of a once-in-a-century event. Sci. Adv. 9, eadf5493. https://doi.org/10.1126/sciadv.adf5493.

Putirka, K.D., 2005. Igneous thermometers and barometers based on plagioclase liquid equilibria: tests of some existing models and new calibrations. Am. Mineral. 90, 336–346. https://doi.org/10.2138/am.2005.1449.

Ribó, M., Cronin, S.J., Garvin, J., Yeo, I.A., Clare, M.A, Watson, S.J., Sielfeld, G., Hunt, J., Slayback, D., Park, S.H., Kang, S.G., Choi, Y., Jung, J., Yoo, J., Hutton, B., White, J.D.L., Brenna, M., Makay, K, Manu, M.S., Latu'ila, F., Heni, N, Tuku'afu, P., Kula, T., (in review). Time-series insights of the geomorphologic evolution of the Hunga submarine caldera. Nat. Geosci.

Schellart, W.P., Lister, G.S., Toy, V.G., 2006. A late cretaceous and cenozoic reconstruction of the Southwest Pacific region: tectonics controlled by subduction and slab rollback processes. Earth. Sci. Rev. 76, 191–233. https://doi.org/10.1016/j.earscirev.2006.01.002.

Seabrook, S., Mackay, K., Watson, S.J., Clare, M.A., Hunt, J.E., Yeo, I.A., Lane, E.M., Clark, M.R., Wysoczanski, R., Rowden, A.A., 2023. Volcaniclastic density currents explain widespread and diverse seafloor impacts of the 2022 Hunga Volcano eruption. Nat. Commun. 14, 7881. https://doi.org/10.1038/s41467-023-43607-2.

Self, S., Sparks, R., 1978. Characteristics of widespread pyroclastic deposits formed by the interaction of silicic magma and water. Bull. Volcanol. 41, 196–212. https://doi.org/10.1007/BF02597223.

Simkin, T., Siebert, L., 1994. Volcanoes of the world: a regional directory, gazetteer and chronology of volcanism during the last 10,000 years. Global Volcanism Program, 2nd ed. Smithsonian Institution, Washington, DC.

Smith, I.E., Price, R.C., 2006. The Tonga–Kermadec arc and Havre–Lau back-arc system: their role in the development of tectonic and magmatic models for the western Pacific. J. Volcanol. Geotherm. Res. 156, 315–331. https://doi.org/10.1016/j.jvolgeores.2006.03.006.

Sparks, S.R., Sigurdsson, H., Wilson, L., 1977. Magma mixing: a mechanism for triggering acid explosive eruptions. Nature 267, 315–318. https://doi.org/10.1038/267315a0.

Stormer Jr, J.C., Nicholls, J., 1978. XLFRAC: a program for the interactive testing of magmatic differentiation models. Comput. Geosci. 4, 143–159. https://doi.org/10.1016/0098-3004(78)90083-3.

Suzuki, Y.J., Martínez Montesinos, B., Costa, A., 2025. Numerical simulations reveal the dynamics of the most intense eruption of Hunga Tonga in January 2022. Bull. Volcanol. 87, 119. https://doi.org/10.1007/s00445-025-01919-9.

Tarumi, K., Yoshizawa, K., 2023. Eruption sequence of the 2022 Hunga Tonga-Hunga Ha'apai explosion from back-projection of teleseismic P waves. Earth. Planet. Sci. Lett. 602, 117966. https://doi.org/10.1016/j.epsl.2022.117966.

Ubide, T., Larrea, P., Becerril, L., Galé, C., 2022. Volcanic plumbing filters on ocean-island basalt geochemistry. Geology 50, 26–31. https://doi.org/10.1130/G49224.1.

Vömel, H., Evan, S., Tully, M., 2022. Water vapor injection into the stratosphere by Hunga Tonga-Hunga Ha'apai. Science 377, 1444–1447. https://doi.org/10.1126/science.Abq2299.

Van Eaton, A.R., Lapierre, J., Behnke, S.A., Vagasky, C., Schultz, C.J., Pavolonis, M., Bedka, K., Khlopenkov, K., 2023. Lightning rings and gravity waves: insights into the giant eruption plume from Tonga's Hunga Volcano on 15 January 2022. Geophys. Res. Lett. 50. https://doi.org/10.1029/2022GL102341 e2022GL102341.

Vaughan, R.G., Webley, P.W., 2010. Satellite observations of a surtseyan eruption: hunga Ha'apai, Tonga. J. Volcanol. Geotherm. Res. 198, 177–186. https://doi.org/10.1016/j.jvolgeores.2010.08.017.

Venzke, E., Sennert, S.K., Wunderman, R., 2009. Reports from the Smithsonian's Global Volcanism Network, March 2009. Bull. Volcanol. 71, 831–832. https://doi.org/10.1007/s00445-009-0307-5.

Wei, L., Pan, X., Trasatti, E., Ao, M., Liu, S., Tolomei, C., Liu, G., Ventura, G., 2025. Deformation and morphological changes before the 2021–2022 explosive eruption at Hunga Tonga-Hunga Ha'apai submarine caldera revealed by satellite remote sensing. Bull. Volcanol. 87, 17. https://doi.org/10.1007/s00445-025-01804-5.

Wu, J., Cronin, S.J., Brenna, M., Park, S., Pontesilli, A., Ukstins, I.A., Adams, D., Paredes-Mariño, J., Hamilton, K., Huebsch, M., González-García, D., Firth, C., White, J.D.L., Nichols, A.R.L., Plank, T., Vongsvivut, J., Klein, A., Ramos, F., Latu'ila, F., Kula, T., 2025. Low sulfur emissions from 2022 Hunga eruption due to seawater–magma interactions. Nat. Geosci. 18, 518–524. https://doi.org/10.1038/s41561-025-01691-7.

Wu, J., Pontesilli, A., Brenna, M., Cronin, S.J., Park, S., Paredes-Mariño, J., Hamilton, K., Ribó, M., Adams, D., Huebsch, M., 2026. A cautionary tale of disequilibria in microlite-melt evolution driven by fast crystallization kinetics: Implications for modeling volcanic processes. Earth. Planet. Sci. Lett. doi:10.1016/j.epsl.2026.120052 in press.